Decoupled Predictive Current Control With Duty-Cycle Optimization of a Grid-Tied Nine-Switch Converter Applied to an Induction Generator

Paulo Roberto Ubaldo Guazzelli, Stefan Thiago Cury Alves dos Santos, Allan Gregori de Castro,
William César de Andrade Pereira, Carlos Matheus Rodrigues de Oliveira,
José Roberto Boffino de Almeida Monteiro, *Member, IEEE*, and Manoel Luís de Aguiar

***Abstract*—The nine-switch converter (NSC) was developed aiming at the reduction in the number of power converter switches in multiport systems, such as variable-speed drives for power generation. Among the possible control techniques for the NSC, finite-control-set model-predictive control (FCS-MPC) stands out due to its fast dynamics and easy incorporation of system restrictions. However, converters with many switching possibilities and control goals increase the computational burden and the cost function complexity. Moreover, FCS-MPC can present high ripple values in the system outputs. This article proposes a decoupled predictive current control with duty-cycle optimization (PCC-DD) for the NSC, which decouples the control of an induction generator from the grid control. The separation between grid and generator controls decreases the enumeration of voltage vectors to be performed, reducing computational burden. Then, duty-cycle calculations are responsible for reducing torque and active power ripples. Experimental results show that PCC-DD provides lower ripple factors for the desired variables when compared to the approach with a concentrated cost function. The main contribution is a better steady-state performance with a lower computational burden. Therefore, PCC-DD is a suitable low-ripple technique for NSC control and for application to power generation with variable-speed generators.**

***Index Terms*—Duty-cycle optimization, nine-switch converter (NSC), predictive current control, squirrel cage induction generator (SCIG).**

I. Introduction

THE reduction in the number of switches in power converters has been a topic of interest for the sake of cost and size reduction [1]. Among the multiport converters linked to the subject, the nine-switch converter (NSC) appears as an alternative for the replacement of the back-to-back converter, as it reduces the number of switches from 12 to nine [2]. The NSC connects two three-phase ac systems with different or equal frequency and amplitude voltages through only one dc bus [3], allowing independent control of them. The converter, seen in Fig. 1, can either power two ac loads independently from a single dc bus, such as electric vehicle traction [4], or transfer power from one ac system to another, through the dc bus, such as uninterrupted power supply systems [3], distributed generation systems [5], power conditioners [6], and power generation systems [2], [7], [8]. In these cases, one ac side acts as a rectifier, and the other as an inverter. In Fig. 1, the upper port is defined as the rectifier, and the lower port is defined as the inverter.

The development of the NSC requires the application of high-performance techniques for its control and driving, such as pulsewidth modulation (PWM) and space vector PWM with linear controllers [9], [10], the sliding-mode technique [11], and the finite-control-set model-predictive control (FCS-MPC) [12]. The latter one stands out for its fast dynamics, reduced to nonexistent factors for adjustment and easy incorporation of nonlinearities and system restraints [13].

Electronic switches are the base of power converters. Since they operate in a discrete ON/OFF mode, we can map every possible combination of switching states the converter may assume. FCS-MPC uses this information to predict the behavior of the controlled system for each one of the possible states of the converter, and then, it chooses the one that minimizes a desired cost function [14]. FCS-MPC has been applied to a variety of power converters, as in three-phase inverters for motor control [15], in static compensators [16], in high-voltage dc transmission systems [17], and in wind power generation, in back-to-back configuration [18].

For the control of machine drives, the predictive torque control (PTC) and the predictive current control (PCC) are prominent. The former has a lower torque ripple, but a higher current ripple and a weighting factor that needs to be adjusted, while the latter

---

Manuscript received January 25, 2021; revised June 21, 2021; accepted September 15, 2021. Date of publication September 24, 2021; date of current version November 30, 2021. This work was supported in part by the Conselho Nacional de Desenvolvimento Científico e Tecnológico and in part by the Coordenação de Aperfeiçamento de Pessoal de Nível Superior (Finance Code 001). Recommended for publication by Associate Editor J. Rodriguez. *(Corresponding author: Paulo Roberto Ubaldo Guazzelli.)*

Paulo Roberto Ubaldo Guazzelli, Stefan Thiago Cury Alves dos Santos, José Roberto Boffino de Almeida Monteiro, and Manoel Luís de Aguiar are with the School of Engineering of São Carlos, University of São Paulo, São Carlos 13566-590, Brazil (e-mail: paulo.ubaldo@usp.br; stefan.santos@usp.br; jrm@sc.usp.br; aguiar@sc.usp.br).

Allan Gregori de Castro is with the School of Engineering of São Carlos, University of São Paulo, São Carlos 13566-590, Brazil, and also with Tecumseh Products Company, São Carlos 13565-090, Brazil (e-mail: allangregori@usp.br).

William César de Andrade Pereira is with WEG Drives and Controls, Jaraguá do Sul 89256-900, Brazil (e-mail: williamwcap@gmail.com).

Carlos Matheus Rodrigues de Oliveira is with the Federal University of Technology—Paraná, Apucarana 86812-460, Brazil (e-mail: carlosoliveira@utfpr.edu.br).

Color versions of one or more figures in this article are available at https://doi.org/10.1109/TPEL.2021.3115049.

Digital Object Identifier 10.1109/TPEL.2021.3115049

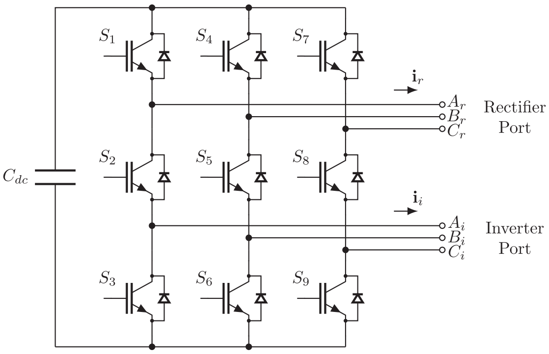

Fig. 1. Nine-switch ac–ac converter.

does not present weighting factors and has a lower current ripple, but with a higher computational burden and torque ripple [19]. Regarding grid-tied converters, the main approaches are the PCC and the predictive power control (PPC) [20].

A number of authors have shown interest in research for FCS-MPC on the adjustment of the weighting factors, the extension of horizons for prediction, the investigation of the discretization methods, and also on the improvement of the steady-state performance [21], [22], which is the focus of this article. These improvements influence another important aspect that is the computational burden for real-time implementation [13].

It is acknowledged that classical FCS-MPC presents high ripples in steady state, due to the application of only one voltage vector per cycle of control [23]. In order to overcome this and improve the PTC of an induction motor with a two-level voltage inverter, the literature has proposed choosing not only the optimal vector but also its optimal time of application, in a duty-cycle way, with the remaining time fulfilled by the null vector [24]. The duty-cycle optimization has also been applied to the two-level voltage inverter in the PPC of active front-end rectifiers [25] and in the PCC of grid-connected inverters with LCL filters [26]. The two-vector technique was also used for PPC of a grid-tied inverter [23].

The advantages of FCS-MPC endorse its application in NSC control. However, even though there are two different systems connected to the NSC, the first proposals of MPC techniques for the NSC had a single cost function merging the control of each port and without duty-cycle calculation. An MPC with a single cost function is applied to the NSC in [20]. An evaluation of 27 switching states for a single cost function with both port controls can be seen for the current control of a current-source NSC in [27] and for the power control of an NSC in [28]. Gulbudak and Santi [29] managed to use only 15 of the 27 voltage vectors in the control. However, the predictive voltage control of two independent RL loads was still combined into a single cost function. The same features were seen in the predictive PTC of two induction motors by Gulbudak and Gokdag [12]. In this case, there were also weighting factors to be adjusted because of the flux errors. In [30], a single cost function combined a PCC and a dc voltage predictive control, at the expense of a weighting factor for the adjustment of the NSC applied to a power quality conditioner.

Nevertheless, merging the objectives into a single cost function can be considered counterproductive. The squirrel cage induction generator (SCIG) control and the grid control are separate structures, whose performance should not be influenced by each other. In a system with the back-to-back converter, for instance, they are controlled separately. If both ports are merged into a single cost function for the NSC, the performance of the lower valued system will be deteriorated in favor of the system with larger variables, because it will have a greater influence in the final value of the cost function of FCS-MPC. The design of a weighting factor for this issue would be complex, since the favoring is not constant, because the magnitude of each variable will change between different points of operation. Additionally, a single cost function does not allow us to look at the vectors for each port individually but rather to look to the pairs of vectors, which increases the enumeration and, therefore, the burden of the system.

The decoupling of the cost functions has been addressed by Guazzelli *et al.* [31], where the decoupling improved the performance on the grid side and reduced it on the generator side. Following this, a decoupled predictive control was applied to the NSC connected to two RL loads on the ac ports, powered by a dc source in the dc bus port [32].

Based on the above discussions, this article focuses on the improvement of generator torque and grid active power ripple factors in the steady state of the FCS-MPC applied to the NSC, with reduction on the computational burden of the technique. This article proposes a decoupled PCC with duty-cycle optimization for the NSC in the power generation, with an SCIG. The PCC technique was chosen for both port controls. One PCC loop controls the SCIG, while the other controls the dc bus voltage of the NSC by means of active power injection. The duty-cycle optimization on the generator current aims at a torque ripple reduction, while the duty-cycle optimization on the grid current aims at an active power ripple reduction. This approach not only reduces the evaluated vector to seven at each time step, reducing significantly the computational burden, but also lowers the torque and active power ripple factors in steady state. The following contributions are emphasized.

1) The decoupling of generator and grid controllers, which avoided the variable favoring from conventional FCS-MPC, reduced the vector enumeration and thus provided a lower computational burden.
2) The duty-cycle optimization based on torque and voltage ripple minimization, which improved the steady-state torque and active power performance of the system, as shown in experimental results, with a computational burden is still lower than the one from the conventional FCS-MPC.

The rest of this article is organized as follows. Section II describes the modeling of the NSC, of the SCIG, and of the three-phase grid. Section III presents the basic implementation of PCC on both ports of the NSC, while the three considered PCC methods are explained in Section IV: the concentrated PCC, the decoupled PCC, and the decoupled PCC with duty-cycle calculation. Section V provides the experimental results of the

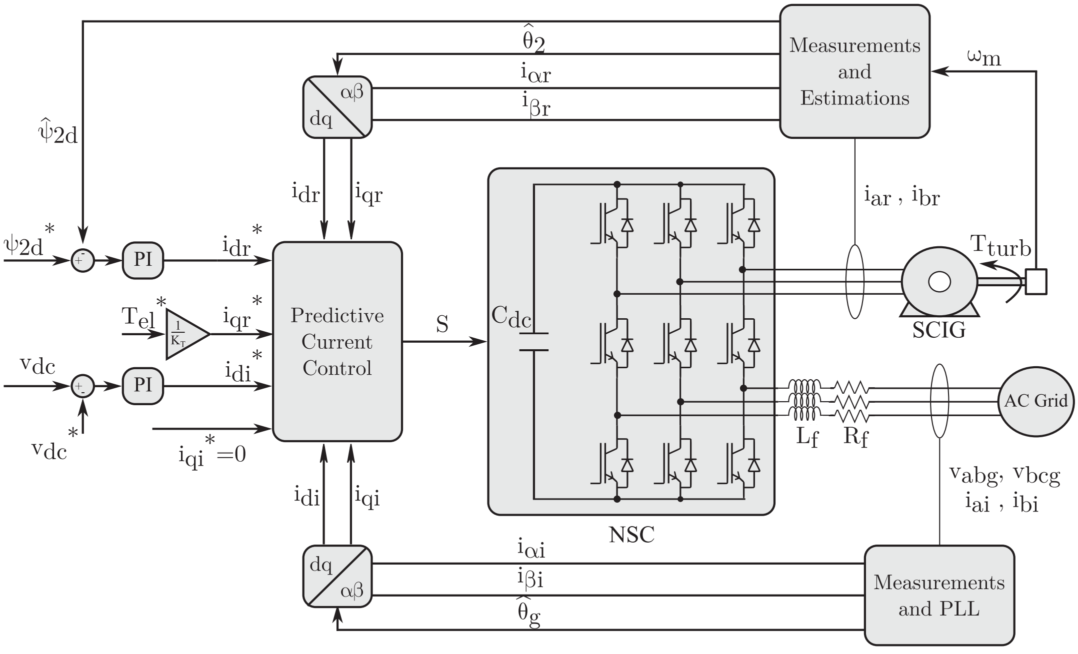

Fig. 2. Diagram of the NSC connected to the SCIG and to the grid.

conventional and proposed control methods. Finally, Section VI concludes this article.

II. System Modeling

The diagram of the NSC control can be seen in Fig. 2. The NSC superior port, called the rectifier, connects to the SCIG, with current measurement. The NSC inferior port, named as inverter, connects to the grid through an L filter, with voltage and current measurements. The rectifier/SCIG current is given by $\mathbf{i}_r$, the inverter/grid current is given by $\mathbf{i}_i$, and ω_m is the SCIG mechanical speed.

A. Nine-Switch Converter

The NSC has nine switches. Since each phase of the ac terminals connects either to $+v_{\mathrm{dc}}$ or to the ground, each leg of the converter must have two switches turned ON and one turned OFF. This restriction results in 27 different combinations, or voltage vectors, according to Table IV in the Appendix.

At each port, there are eight possible voltage vectors, $\mathbf{v}_0$–$\mathbf{v}_7$, which have the coordinates in the $\alpha\beta$ reference frame as a function of the dc-bus voltage. These coordinates are listed in Table I. There are six active and two null voltage vectors, as seen in Fig. 3. Thus, NSC requires twice the dc-bus voltage of the back-to-back converter for the same output ac voltage [3].

From the 27 switching state combinations, 12 apply an active voltage vector in one port and a null one in the other, denominated here as pure, while 12 apply an active voltage vector on both ports, denominated here as mixed, and three apply null voltage vectors in both ports, as highlighted in Table IV in the Appendix.

TABLE I
Coordinates of Each Voltage Vector in the $\alpha\beta$ Reference Frame

Vector	v_α	v_β	Amplitude
$\mathbf{v}_0$	0	0	0
$\mathbf{v}_1$	$\frac{2}{3}v_{dc}$	0	$\frac{2}{3}v_{dc}$
$\mathbf{v}_2$	$\frac{1}{3}v_{dc}$	$\frac{\sqrt{3}}{3}v_{dc}$	$\frac{2}{3}v_{dc}$
$\mathbf{v}_3$	$-\frac{1}{3}v_{dc}$	$\frac{\sqrt{3}}{3}v_{dc}$	$\frac{2}{3}v_{dc}$
$\mathbf{v}_4$	$-\frac{2}{3}v_{dc}$	0	$\frac{2}{3}v_{dc}$
$\mathbf{v}_5$	$-\frac{1}{3}v_{dc}$	$-\frac{\sqrt{3}}{3}v_{dc}$	$\frac{2}{3}v_{dc}$
$\mathbf{v}_6$	$\frac{1}{3}v_{dc}$	$-\frac{\sqrt{3}}{3}v_{dc}$	$\frac{2}{3}v_{dc}$
$\mathbf{v}_7$	0	0	0

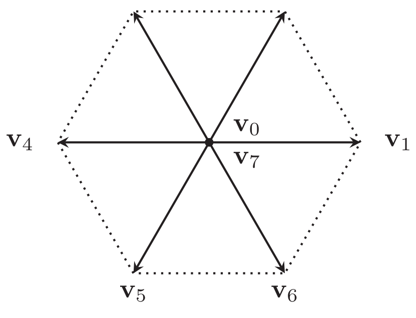

Fig. 3. Voltage vectors in the $\alpha\beta$ reference frame.

B. SCIG Model

Let the SCIG model be oriented in the rotor flux synchronous reference frame [33]. The stator currents are given by $\mathbf{i}_r$ since they are connected to the rectifier port of the NSC. Therefore

$$\mathbf{i}_r = i_{dr} + j i_{qr} = e^{j\theta_2}(i_{\alpha r} + j i_{\beta r}) \tag{1}$$

where θ_2 is the rotor flux angle and j is the complex operator. The rotor flux is given only as $\psi_2 = \psi_{2d}$. The SCIG model is then given by (2), where R_1 and R_2 are the stator and rotor resistances, respectively, L_1 and L_2 are the stator and rotor inductances, respectively, and L_H stands for the mutual inductance. Variable p denotes the number of pole pairs. For simplification, let $\sigma := 1 - \frac{L_H^2}{L_1 L_2}$, and ω_2 is the rotor flux speed, given by (3)

$$\frac{d\mathbf{i}_r}{dt} = \frac{\mathbf{v}_1}{\sigma L_1} - \left(\frac{R_2 L_H^2}{\sigma L_1 L_2^2} + \frac{R_1}{\sigma L_1} + j\omega_2\right)\mathbf{i}_r + + \frac{L_H}{\sigma L_1 L_2}\left(\frac{R_2}{L_2} - jp\omega_m\right)\psi_2 \tag{2a}$$

$$\frac{d\psi_2}{dt} = \frac{R_2 L_H}{L_2}\mathbf{i}_r - \frac{R_2}{L_2}\psi_2 \tag{2b}$$

$$\omega_2 = p\omega_m + \frac{R_2 L_H}{L_2}\frac{i_{qr}}{\psi_{2d}}. \tag{3}$$

There are two outer variables for the SCIG control. One proportional–integral (PI) controller is responsible for control of the rotor flux amplitude and determines the current reference i_{dr}. On the other hand, the current reference i_{qr} is calculated from the torque reference T_{el}^* directly through

$$i_{qr}^* = \frac{1}{K_T}\cdot T_{el}^* = \frac{2L_2}{3pL_H\hat{\psi}_{2d}}\cdot T_{el}^*. \tag{4}$$

The rotor flux angle and amplitude are calculated from (2b) and (3), allowing for the conversion of the reference currents from the $\alpha\beta$ to the dq frame.

C. Grid Model

The grid model was oriented in the grid voltage $\mathbf{v}_g$. If θ_g is the grid angle, then

$$\mathbf{i}_i = i_{di} + j i_{qi} = e^{j\theta_g}(i_{\alpha i} + j i_{\beta i}). \tag{5}$$

The three-phase grid is connected to the NSC by an L filter, with R_f resistance and L_f inductance; therefore, the inverter port modeling is given by

$$\frac{d\mathbf{i}_i}{dt} = \frac{1}{L_f}\left(\mathbf{v}_i - \mathbf{v}_g - R_f\mathbf{i}_i - j\omega_g\mathbf{i}_i\right) \tag{6}$$

where ω_g is the grid angular frequency.

The grid control outer loop is shown in Fig. 2. The inverter port of the NSC must transfer energy between the dc bus and the grid so the dc-bus voltage is maintained at the reference. Then, a PI controller determines the current reference on the d-axis i_{di}^*, while the current reference i_{qi}^* is set to zero. A phase-locked loop (PLL) is responsible for finding θ_g and ω_g, for the reference frame conversion of (5). A synchronous reference frame PLL with moving average filter was employed, as it is a standard PLL for three-phase applications [34], with good performance under unbalanced voltage conditions [35].

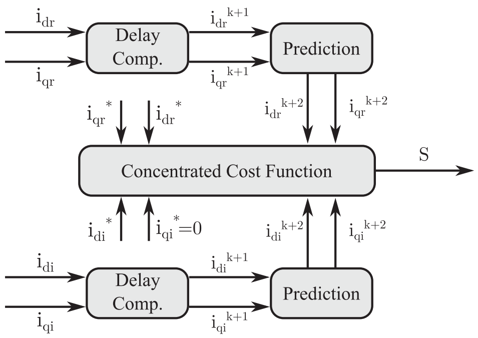

Fig. 4. Diagram of PCC-C for the NSC.

III. PREDICTIVE CURRENT CONTROL

A. Inverter Port PCC

The prediction of the grid currents is shown in (7) in the dq reference frame. This is derived from the grid model in (6) and is calculated for each voltage vector V_n of the NSC. The discretization time is represented by t_D, using the forward Euler discretization method

$$\mathbf{i}_i^{k+1} = \mathbf{i}_i^k + \frac{t_D}{L_f}\left(\mathbf{v}_n - \mathbf{v}_g^k - R_f\cdot\mathbf{i}_i^k - j\omega_g L_f\mathbf{i}_i^k\right). \tag{7}$$

The predicted grid currents and their respective control references are used for the cost function minimization, as in (8). The quadratic function was chosen for error calculation over the absolute value of the errors, as it possesses better performance and stability guarantees [36]

$$g_{\mathrm{inv}_n} = \left(i_{di}^* - \hat{i}_{di_n}^{k+1}\right)^2 + \left(i_{qi}^* - \hat{i}_{qi_n}^{k+1}\right)^2. \tag{8}$$

B. Rectifier Port PCC

The following equation predicts the SCIG dq currents, based on the model of (2), for each voltage vector V_n mapped

$$\mathbf{i}_r^{k+1} = \mathbf{i}_r^k + t_D\left(\frac{L_H}{\sigma L_1 L_2}\left(\frac{R_2}{L_2} - jp\omega_m^k\right)\hat{\psi}_{2d}^k + \frac{\mathbf{v}_n}{\sigma L_1} + - \left(\frac{R_2 L_H^2}{\sigma L_1 L_2^2} + \frac{R_1}{\sigma L_1} + j\omega_2^k\right)\mathbf{i}_r^k\right). \tag{9}$$

The cost function below follows the same structure as (8)

$$g_{\mathrm{rect}_n} = \left(i_{dr}^* - \hat{i}_{dr_n}^{k+1}\right)^2 + \left(i_{qr}^* - \hat{i}_{qr_n}^{k+1}\right)^2. \tag{10}$$

IV. VOLTAGE VECTOR EVALUATION

The modeling of the possible voltage vectors of the NSC is fundamental for the steps of prediction and cost function evaluation of PCC. The predictive controls in literature for NSC have been proposed with the scheme depicted in Fig. 4. The controls of the inverter and of the rectifier ports are combined into a single cost function, as in (11). The control scheme with two PCC combined was hereby named as PCC-C. Since both cost functions are in the same unit (A), there are no weighting factors needed. As seen from Fig. 4, this control scheme requires

Algorithm 1: Code Execution for PCC-C

```
Measurements of $\mathbf{i_r}$, $\omega_m$, $\mathbf{i_i}$, $\mathbf{v_g}$, and $v_{dc}$
Estimation of $\theta_2$, $\psi_{2d}$, and $\theta_g$
Synchronous reference frames conversion
Delay compensation: (7) and (9)
for each pure or null voltage vector of Table IV do
  Prediction of currents: (7) and (9) at $k+2$
  Cost function calculation: (8), (10), and (11) at $k+2$
  Update of the optimal voltage vector
end for
return Optimal voltage vector
```

the delay compensation, which is a preprediction with the previous voltage vector [37]. As a result, the cost function uses the variables predicted at the $(k+2)$th step [38], modifying (8) and (10)

$$g_{\text{conc}}(i) = g_{\text{rect}}(i) + g_{\text{inv}}(i). \tag{11}$$

The PCC-C implementation is represented in Algorithm 1, for one time step of control.

The implementation of this technique requires the evaluation of the 27 switching combinations in Table IV, which is a relatively costly task for embedded systems. Even if only the pure voltage vectors and a null one are assumed (constituting 13 voltage vectors), the computational burden of the technique is still significant. This reduced set of voltage vectors was hereby named the PCC-CR. Another potential setback of this technique is that, even if all the variables in the cost function are in A, the values of the currents are different. Therefore, the port with the highest current will be prioritized by the PCC, leading to an inferior performance of the port with the lowest current.

A. Decoupling of the Cost Functions

The NSC can be understood as two inverters [39]: if the three lower switches are turned ON, the six upper ones constitute a three-phase two-level inverter, and when the three upper switches are turned ON, the same behavior is observed in the six lower switches. This feature prompted the development of a decoupled PCC, named as PCC-D, which opposes the usual merging of generator and grid cost functions into a single function. Instead, PCC-D computes the cost functions g_{rect} and g_{inv} every other step; hence, only the SCIG control is evaluated at one time step, and in the following step, only the grid control is executed. As a result, only seven possible switching states, the six active voltage vectors and one null vector from Table I, are necessary for evaluation. Fig. 5 illustrates the difference between PCC-D and earlier reported PCC-C.

Noteworthy here is that in this approach, each PCC will operate with half of the discretization time, and each predicted vector in the cost function has a mean value equal to half, when compared to the vectors in PCC-C. The diagram of PCC-D is shown in Fig. 6. A multiplexer switches from one control to another every step. Consequently, there is a low computational burden not only because of the low quantity of voltage vectors, but also due to the control being split.

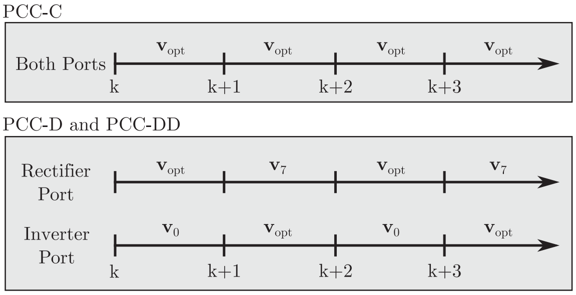

Fig. 5. Discrete-time comparison between PCC-C and PCC-D applied to the NSC, for the same time base.

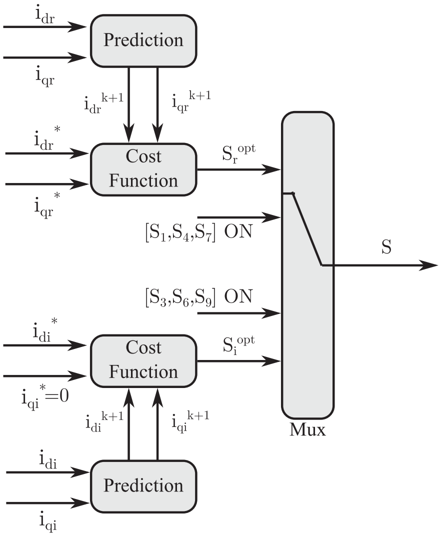

Fig. 6. Diagram of PCC-D for the NSC.

PCC-D is implemented according to Algorithm 2.

Another advantage of this scheme is that the null vector period creates a time gap, which eliminates the delay from the prediction stage. Thus, compensation is not needed, as in conventional FCS-MPC implementation [37].

Regarding ports with different current values, now the port with the lowest current is not deprecated by the port with the highest value. On the other hand, the highest current port is not favored anymore by this feature of PCC-C.

B. Duty-Cycle Optimization

Aiming at improvements in steady-state operation for both system ports, this work introduces the decoupled predictive current control with duty-cycle optimization (PCC-DD), which considers not only the application of the voltage vectors depicted in Fig. 3, but also a dwell time t^{opt} of it. The remaining time is filled by the null voltage vector, which is constituted of an optimal duty cycle δ_{opt} that needs to be found. As such, the vector on each port has a correspondent dwell time that needs calculating, t_r^{opt} and t_i^{opt}, in accordance with the variables for minimization.

1) Torque Ripple Minimization: In order to influence the SCIG torque ripple, one must act on the i_{qr} current. From

Algorithm 2: Code Execution for PCC-D.

```
Measurements of $\mathbf{i_r}$, $\omega_m$, $\mathbf{i_i}$, $\mathbf{v_g}$, and $v_{dc}$
Estimation of $\theta_2$, $\psi_{2d}$, and $\theta_g$
Synchronous reference frames conversion
switch Port do
  case Rectifier
    for each voltage vector of Table I do
        Prediction of currents: (7)
        Cost function calculation: (8)
        Update of the optimal voltage vector
    end for
    return Optimal voltage vector
    Port=Inverter
    break
  case Inverter
    for each voltage vector of Table I do
        Prediction of currents: (9)
        Cost function calculation: (10)
        Update of the optimal voltage vector
    end for
    return Optimal voltage vector
    Port=Rectifier
    break
end switch
```

the dead-beat principle, the future current can be calculated as follows:

$$i_{qr}^{k+1} = i_{qr}^{k} + \Delta_r^n t_r^{\text{opt}} + \Delta_r^0 (t_D - t_r^{\text{opt}}) \mapsto i_{qr}^* \tag{12}$$

where Δ_r^n is the derivative term of SCIG in terms of the j voltage vector, and Δ_r^0 is the derivative term regarding the null voltage vector, for the system at the rectifier port

$$\Delta_r^0 = -\frac{R_1 L_2^2 + R_2 L_H^2}{\sigma L_1 L_2^2} i_{qr} - \omega_2 i_{dr} - \frac{L_H p \omega_m}{\sigma L_1 L_2} \hat{\psi}_{2d} \tag{13}$$

$$\Delta_r^n = \Delta_r^0 + \frac{v_{q_n}}{\sigma L_1}. \tag{14}$$

The optimal time t_r^{opt} and the optimal duty cycle δ_r^{opt} are then obtained from (12), as follows:

$$\delta_r^{\text{opt}} = \frac{t_r^{\text{opt}}}{t_D} = \frac{i_{qr}^* - i_{qr}^k - \Delta_r^0 t_D}{t_D (\Delta_r^n - \Delta_r^0)}. \tag{15}$$

2) Active Power Ripple Minimization: An analog approach was conducted on the inverter port. However, since there is an interest in the minimization of the active power ripple, the duty-cycle calculation must depend on the i_{di} current. Therefore

$$\delta_i^{\text{opt}} = \frac{i_{di}^* - i_{di}^k - \Delta_i^0 t_D}{(\Delta_i^n - \Delta_i^0) t_D} \tag{16}$$

where the derivative terms are calculated as

$$\Delta_i^0 = \frac{-v_{dg} - R_f i_{di}}{L_f} + \omega_g i_{qi} \tag{17}$$

$$\Delta_i^n = \Delta_i^0 + \frac{v_{dn}}{L_f}. \tag{18}$$

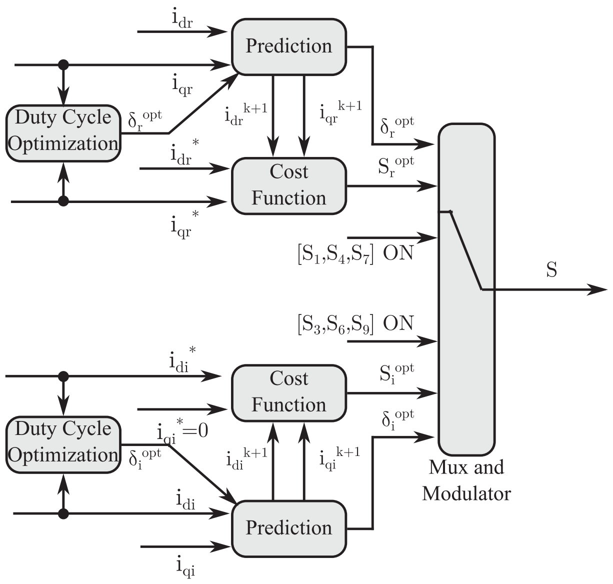

Fig. 7. Diagram of PCC-DD for the NSC.

These optimal duty cycles require its inclusion in the prediction stage of (7) and (9), for each considered j voltage vector. The new prediction equations are depicted as follows:

$$\mathbf{i}_i^{k+1} = \mathbf{i}_i^k + \frac{t_D}{L_f} \left(\delta_i^{\text{opt}} \mathbf{v}_n - \mathbf{v}_g^k - R_f \cdot \mathbf{i}_i^k - j\omega_g L_f \mathbf{i}_i^k \right) \tag{19}$$

$$\mathbf{i}_r^{k+1} = \mathbf{i}_r^k + t_D \Bigg(\frac{L_H}{\sigma L_1 L_2} \left(\frac{R_2}{L_2} - jp\omega_m^k \right) \hat{\psi}_{2d}^k + \frac{\delta_r^{\text{opt}} \mathbf{v}_n}{\sigma L_1} + - \left(\frac{R_2 L_H^2}{\sigma L_1 L_2^2} + \frac{R_1}{\sigma L_1} + j\omega_2^k \right) \mathbf{i}_r^k \Bigg). \tag{20}$$

Consequently, PCC-DD has the basic structure of Fig. 7.

Two PCCs still act alternatively, and the steps for duty-cycle calculation are added. A modulator, at the end of the cycle, synthesizes the desired switching state during the optimum time. The modified algorithm for PCC-DD can be seen in Algorithm 3.

V. Results and Discussion

The PCC-D and PCC-DD were implemented using the setup depicted in Fig. 8, as well as the PCC-CR, with the reduced set of voltage vectors. The hardware setup used for experimental validation contains a 73/127-V SCIG and a variable transformer, both connected to the NSC. An induction motor drives the SCIG, and the control algorithms run on a floating-point DSP F28379D from Texas Instruments. The parameters of the system components are in Table V in the Appendix. The dc-bus voltage PI controller gains were adjusted to $K_P = 0.05$ and $K_I = 1.25$, and the flux PI gains were set to $K_P = 40$ and $K_I = 400$. A low-pass filter of 660 Hz was employed for all ac measured currents and voltages, and 60-Hz low-pass filter for the dc-bus voltage.

The three techniques were implemented with the same sampling frequency of 20 kHz, which means a 20-kHz control frequency for PCC-C and a 10-kHz control frequency for PCC-D

Algorithm 3: Code Execution for PCC-DD.

```
Measurements of $\mathbf{i_r}$, $\omega_m$, $\mathbf{i_i}$, $\mathbf{v_g}$, and $v_{dc}$
Estimation of $\theta_2$, $\psi_{2d}$, and $\theta_g$
Synchronous reference frame conversion
switch Port do
  case Rectifier
    for each voltage vector of Table I do
      Optimal duty-cycle calculation: (16)
      Prediction of currents: (19)
      Cost function calculation: (8)
      Update optimal voltage vector and duty cycle
    end for
    return Optimal voltage vector and duty cycle
    Port=Inverter
    break
  case Inverter
    for each voltage vector of Table I do
      Optimal duty-cycle calculation: (15)
      Prediction of currents: (20)
      Cost function calculation: (10)
      Update optimal voltage vector and duty cycle
    end for
    return Optimal voltage vector and duty cycle
    Port=Rectifier
    break
end switch
```

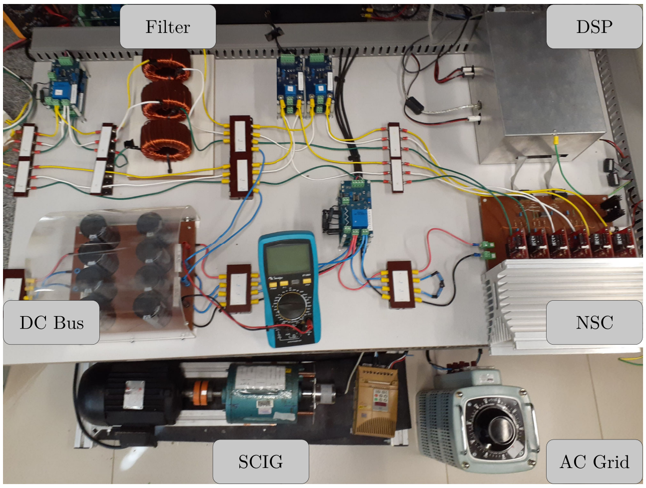

Fig. 8. Hardware setup for experimental validation.

and PCC-DD. The system was tested under a torque reference of 3.5 N · m and a dc voltage reference of 220 V, at the steady-state speed of 1000 r/min. The resulting graphs for the SCIG speed, torque, dq currents, and phase a current are depicted in Fig. 9, for the PCC-C, PCC-D, and PCC-DD, in blue, red, and green, respectively. The torque ripple of PCC-D is greater when compared to PCC-C, while PCC-DD presented the lowest ripple of the three, showing the success of the duty-cycle calculation. In addition, the i_{qr} current ripple decreased significantly for the PCC-DD, according to the minimization performed by (15).

The graphs for the dc bus voltage, grid dq currents, and phase a current are also illustrated in Fig. 9, for the PCC-C, PCC-D, and PCC-DD, in the same colors, for the same experimental condition. PCC-D provided similar ripples for the dq grid current, when compared to PCC-C. An improvement is depicted for PCC-DD, which led to a visible improvement in the phase a current. Furthermore, the reduction in the i_{di} ripple is visible for PCC-DD, because of the optimization in this component.

Additionally, the grid active and reactive powers can be seen in Fig. 9, for the three control techniques considered. It is clear that PCC-C provided the active power with the highest ripple and PCC-DD provided the lowest.

The three techniques were also tested for a torque step change. The torque reference changed from 2.5 to 3.5 N · m, generating the graphs from Fig. 10, at 1000 r/min. All the techniques achieved the new reference, keeping the i_{dr} current constant, as well as the rotor flux amplitude. In order to achieve the new reference, i_{qr} current increased from 4.6 to 6.4 A. The three techniques presented settling times inferior to 2 ms, showing the typical fast dynamics provided by FCS-MPC. The proposed techniques did not deteriorate this advantage.

The grid variables in Fig. 10 show how the grid response is slower than the one from the SCIG, because of the PI controller. The largest input power on the rectifier side raised the dc-bus voltage. The PI controller, therefore, increased the i_{di} current reference. As a result, the direct current changed from 1.2 to 2.4 A, and the active power injected onto the grid changed from 90 to 180 W. Concurrently, i_{qi} and the reactive power were controlled in zero. Again, it can be seen how PCC-DD provided an active power with lower oscillations.

The three control techniques were evaluated for a range of SCIG speeds, at steady state, with a torque reference of 3.5 N · m. Thus, the graphs of Fig. 11 were obtained, which show the ripple factors of the torque and the grid active power of the system, as well as the grid current total harmonic distortion (THD). The results show that PCC-D provided lower active power ripple factors than PCC-C for the whole range of speeds, at the cost of higher torque ripple factors, showing how PCC-C was indeed prioritizing the system with the highest current value. However, PCC-DD lowered both ripple factors against PCC-D and PCC-C, thus effectively reducing the ripple of the variables used for the duty-cycle calculation.

Regarding the grid current THD, PCC-D provided the lowest values for the whole range of speeds, as shown in Fig. 11(c).

The computational burdens of each techniques are seen in Fig. 12. PCC-D also had the lowest computational burden of the three techniques, followed by the PCC-DD. Additionally, Table II provides a detailed look on the execution times of each technique. Through this table, one notes that PCC-D and PCC-DD had faster prediction and cost function stages than PCC-C, which is due to the smaller enumeration of voltage vectors and absence of delay compensation. The difference between PCC-DD and PCC-D execution times is on the account of the duty-cycle calculation. However, the execution time of PCC-DD is still 43% lower than that of the PCC-C. These lower execution times are beneficial since they allow for either a higher sampling time or a cheaper embedded system.

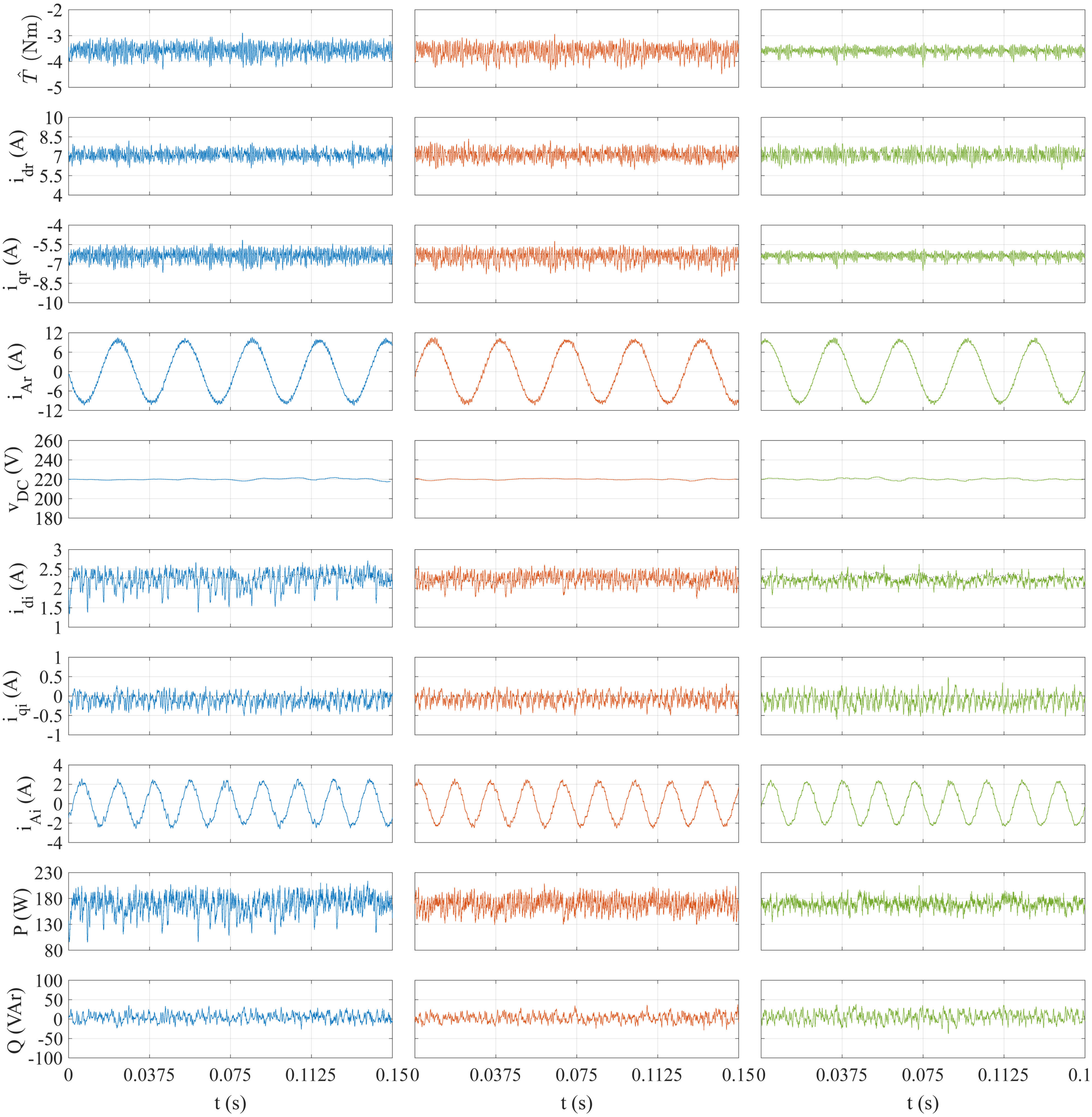

Fig. 9. Steady-state results at 1000 r/min, with torque reference at 3.5 N · m for the PCC-C (blue), PCC-D (red), and PCC-DD (green). Top to bottom: SCIG torque, dq currents, and phase a current; dc-bus voltage, dq grid currents, and phase a grid current; and active and reactive grid powers. Current references in dotted black lines.

TABLE II
EXECUTION TIMES FOR EACH CONTROL TECHNIQUE

Stage	PCC-C	PCC-D	PCC-DD
Conversions and estim.	5.55	5.55	5.55
Outer loops control	1.50	1.50	1.50
Prediction and cost funct.	17.60	5.75	5.75
Duty cycles optim.	—	—	1.30
Total execution time (μs)	24.75	12.80	14.10
Reduction over PCC-C (%)	—	48.3	43.0

Two more features are worth mentioning. The first of them is the presence or absence of voltage modulators. Conventional FCS-MPC does not need them, since it determines the states of each electronic switch directly. However, predictive techniques with duty-cycle optimization, as PCC-DD, require a voltage modulator to synthesize the desired voltage. The other issue to be mentioned is the switching frequency of the system. PCC-C and PCC-D have a variable switching frequency. PCC-DD, however, has a fixed switching frequency. Finally, Table III summarizes the characteristics and advantages addressed in this article, for each technique.

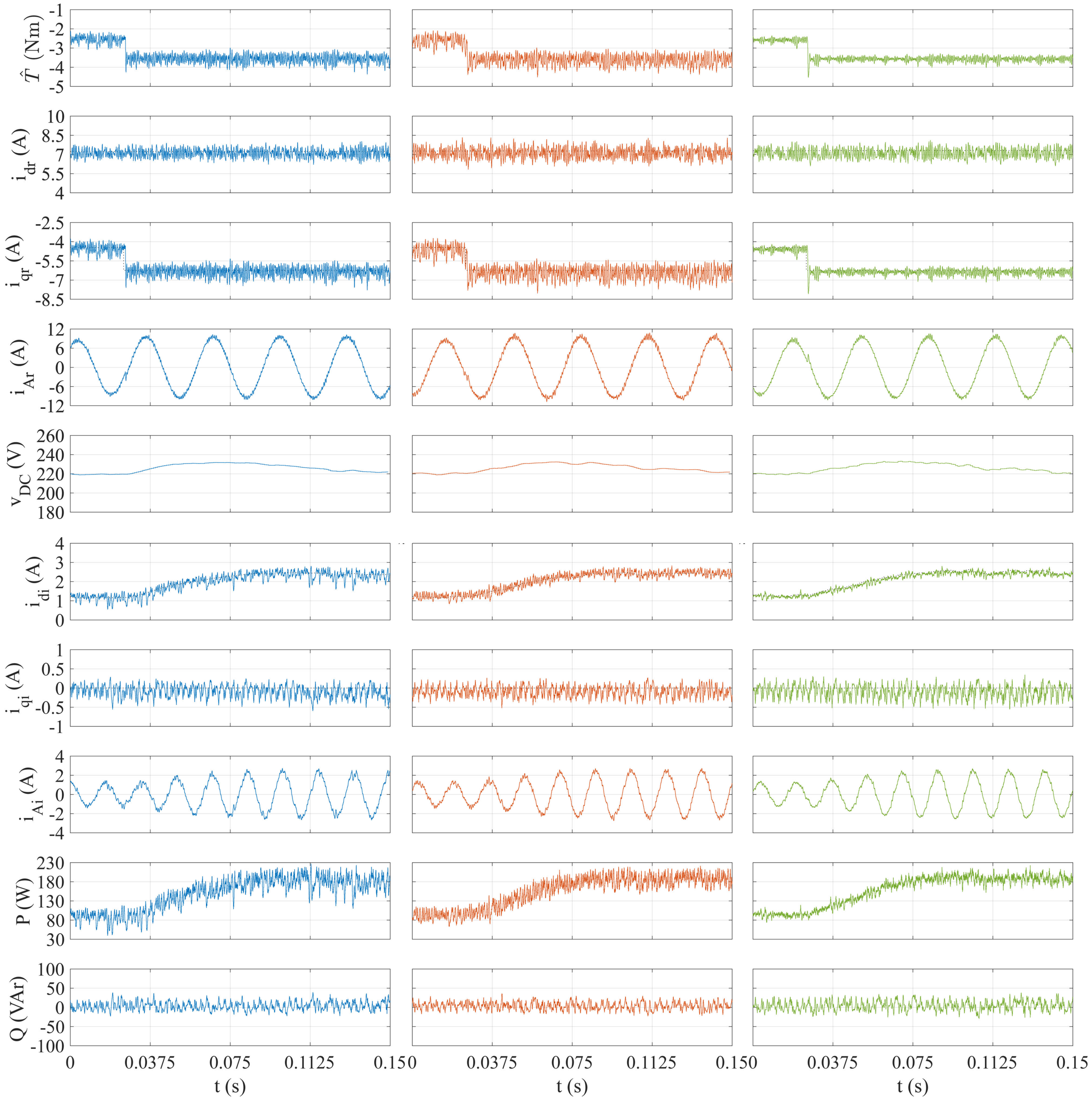

Fig. 10. Dynamic results at 1000 r/min, with a torque step reference from 2.5 to 3.5 N · m for the PCC-C (blue), PCC-D (red), and PCC-DD (green). Top to bottom: SCIG torque, dq currents, and phase a current; dc bus voltage, dq grid currents, and phase a grid current; and active and reactive grid powers. Current references in dotted black lines.

VI. CONCLUSION

The finite switching combinations of the NSC were exploited by MPC theory, for the control of a SCIG and power injection on the grid. The decoupling between generator and grid control was considered in opposition to a concentrated MPC. As a result, one PCC loop controls the SCIG, while the other controls the dc-bus voltage for grid power delivery. Experimental results showed how PCC-D provided a power injection onto the grid with lower ripple factor, at the cost of a higher torque ripple factor in the generator. PCC-D also removed the favoring of the rectifier side over the inverter side and reduced the computational burden by 48%.

In order to overcome the mentioned drawback of PCC-D, the decoupling of the generator and grid controls led to the development of PCC-DD, which employed the duty-cycle calculation in both NSC ports. The duty-cycle calculation of the rectifier-side current minimized the SCIG torque ripple, and the calculation of the grid-side current minimized the active power ripple, independently from one another. Experimental results showed that the ripple factors were effectively reduced for the desired variables, on both ports on the converter. This

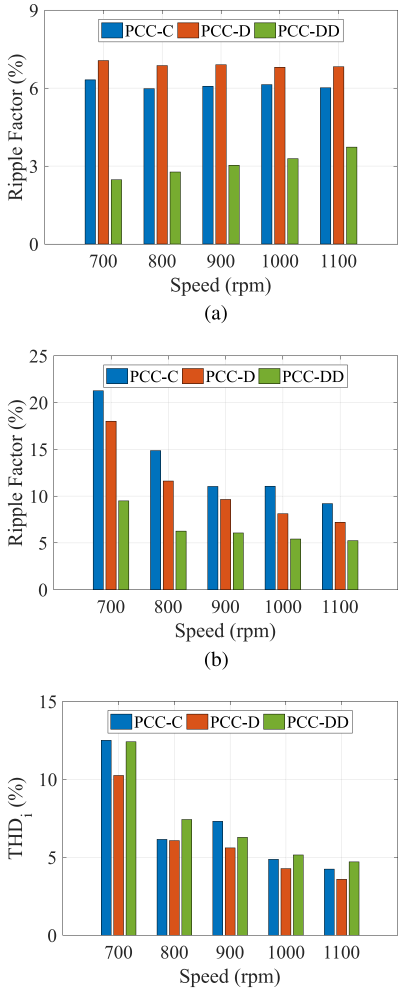

(a)

(b)

(c)

Fig. 11. Comparisons of (a) torque and (b) active power ripple factors and (c) grid current THD for a range of speeds, under the 3.5-N · m torque reference. (a) Torque ripple factor. (b) Active power ripple factor. (c) Grid current THD.

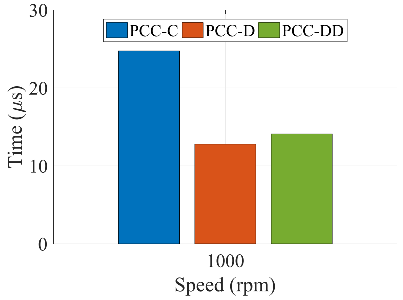

Fig. 12. Computational burden of PCC-C, PCC-D, and PCC-DD.

was achieved with a computational burden still smaller than the one from PCC-C.

A low computational burden is especially important for embedded systems, as it allows for higher sampling times and, therefore, a better performance, or the use of a less powerful embedded system and, therefore, a cheaper system. PCC-D and PCC-DD reduced the vector enumeration by 50% when compared to the PCC-CR, which had an impact on the computational burden of each strategy. The additional calculations of the PCC-DD increased its computational burden when compared to PCC-D, but with a quantity that was still 43% lower than the PCC-CR. These results certify the use of MPC in the NSC control for power generation. This is found through its offering a better performance than the previous applications of FCS-MPC to the NSC regarding computational burden and steady-state performances of torque and active grid power.

TABLE III
SUMMARY OF THE EVALUATED TECHNIQUES

Feature	PCC-C	PCC-D	PCC-DD
Torque ripple	Medial	Highest	Lowest
Active power ripple	Highest	Medial	Lowest
Grid current THD	Highest	Lowest	Highest
Torque dynamics	Fast	Fast	Fast
Computational burden	Highest	Lowest	Medial
Bigger value favoring	Yes	No	No
Voltage modulator	No	No	Yes
Switching frequency	Variable	Variable	Fixed

APPENDIX

TABLE IV
NSC POSSIBLE SWITCHING STATES AND VOLTAGE VECTORS

Switching States	Applied Vector		Type
$[S_{1-9}]$	Rectifier Port	Inverter Port	
[110110110]	$\mathbf{v}_7$	$\mathbf{v}_7$	Null
[110110011]	$\mathbf{v}_2$	$\mathbf{v}_2$	Mixed
[110110101]	$\mathbf{v}_7$	$\mathbf{v}_2$	Pure
[110011110]	$\mathbf{v}_6$	$\mathbf{v}_6$	Mixed
[110011011]	$\mathbf{v}_1$	$\mathbf{v}_1$	Mixed
[110011101]	$\mathbf{v}_6$	$\mathbf{v}_1$	Mixed
[110101110]	$\mathbf{v}_7$	$\mathbf{v}_6$	Pure
[110101011]	$\mathbf{v}_2$	$\mathbf{v}_1$	Mixed
[110101101]	$\mathbf{v}_7$	$\mathbf{v}_1$	Pure
[011110110]	$\mathbf{v}_4$	$\mathbf{v}_4$	Mixed
[011110011]	$\mathbf{v}_3$	$\mathbf{v}_3$	Mixed
[011110101]	$\mathbf{v}_4$	$\mathbf{v}_3$	Mixed
[011011110]	$\mathbf{v}_5$	$\mathbf{v}_5$	Mixed
[011011011]	$\mathbf{v}_0$	$\mathbf{v}_0$	Null
[011011101]	$\mathbf{v}_5$	$\mathbf{v}_0$	Pure
[011101110]	$\mathbf{v}_4$	$\mathbf{v}_5$	Mixed
[011101011]	$\mathbf{v}_3$	$\mathbf{v}_0$	Pure
[011101101]	$\mathbf{v}_4$	$\mathbf{v}_0$	Pure
[101110110]	$\mathbf{v}_7$	$\mathbf{v}_4$	Pure
[101110011]	$\mathbf{v}_2$	$\mathbf{v}_3$	Mixed
[101110101]	$\mathbf{v}_7$	$\mathbf{v}_3$	Pure
[101011110]	$\mathbf{v}_6$	$\mathbf{v}_5$	Mixed
[101011011]	$\mathbf{v}_1$	$\mathbf{v}_0$	Pure
[101011101]	$\mathbf{v}_6$	$\mathbf{v}_0$	Pure
[101101110]	$\mathbf{v}_7$	$\mathbf{v}_5$	Pure
[101101011]	$\mathbf{v}_2$	$\mathbf{v}_0$	Pure
[101101101]	$\mathbf{v}_7$	$\mathbf{v}_0$	Null

TABLE V
SCIG AND GRID PARAMETERS

Parameter	Value	Unit
Nominal torque	6.1	Nm
Nominal speed	1750	rpm
Nominal rotor flux	0.21	V·s
R_s	0.8088	Ω
R_r	0.2648	Ω
L_s and L_r	33.1	mH
L_H	29.5	mH
p	2	—
v_{dc}^*	220	V
C_{dc}	750	μF
L_f	8.5	mH
R_f	0.167	Ω
Line-to-line grid voltage	60	V
Grid frequency	60	Hz

REFERENCES

[1] C. B. Jacobina, M. B. D. R. Correa, A. M. N. Lima, and E. R. C. D. Silva, “AC motor drive systems with a reduced-switch-count converter,” *IEEE Trans. Ind. Appl.*, vol. 39, no. 5, pp. 1333–1342, Sep./Oct. 2003.

[2] C. N. Jibhakate, M. A. Chaudhari, and M. M. Renge, “Reactive power compensation using induction motor driven by nine switch AC-DC-AC converter,” *IEEE Access*, vol. 6, pp. 1312–1320, 2018.

[3] C. Liu, B. Wu, N. R. Zargari, D. Xu, and J. Wang, “A novel three-phase three-leg AC/AC converter using nine IGBTs,” *IEEE Trans. Power Electron.*, vol. 24, no. 5, pp. 1151–1160, May 2009.

[4] M. S. Diab, A. A. Elserougi, A. S. Abdel-Khalik, A. M. Massoud, and S. Ahmed, “A nine-switch-converter-based integrated motor drive and battery charger system for EVs using symmetrical six-phase machines,” *IEEE Trans. Ind. Electron.*, vol. 63, no. 9, pp. 5326–5335, Sep. 2016.

[5] P. C. Loh, L. Zhang, and F. Gao, “Compact integrated energy systems for distributed generation,” *IEEE Trans. Ind. Electron.*, vol. 60, no. 4, pp. 1492–1502, Apr. 2013.

[6] L. Zhang, P. C. Loh, and F. Gao, “An integrated nine-switch power conditioner for power quality enhancement and voltage sag mitigation,” *IEEE Trans. Power Electron.*, vol. 27, no. 3, pp. 1177–1190, Mar. 2012.

[7] G. Wen, Y. Chen, Z. Zhong, and Y. Kang, “Dynamic voltage and current assignment strategies of nine-switch-converter-based DFIG wind power system for low-voltage ride-through (LVRT) under symmetrical grid voltage dip,” *IEEE Trans. Ind. Appl.*, vol. 52, no. 4, pp. 3422–3434, Jul./Aug. 2016.

[8] A. Kirakosyan, M. S. El Moursi, P. Kanjiya, and V. Khadkikar, “A nine switch converter-based fault ride through topology for wind turbine applications,” *IEEE Trans. Power Del.*, vol. 31, no. 4, pp. 1757–1766, Aug. 2016.

[9] F. Gao, L. Zhang, D. Li, P. C. Loh, Y. Tang, and H. Gao, “Optimal pulsewidth modulation of nine-switch converter,” *IEEE Trans. Power Electron.*, vol. 25, no. 9, pp. 2331–2343, Sep. 2010.

[10] S. M. Dehghan Dehnavi, M. Mohamadian, A. Yazdian, and F. Ashrafzadeh, “Space vectors modulation for nine-switch converters,” *IEEE Trans. Power Electron.*, vol. 25, no. 6, pp. 1488–1496, Jun. 2010.

[11] Y. Chen, G. Wen, and Y. Kang, “Sliding mode pulsewidth modulation (SMPWM) for nine-switch converter,” in *Proc. IEEE Int. Symp. Ind. Electron.*, May 2013, pp. 1–6.

[12] O. Gulbudak and M. Gokdag, “Predictive dual-induction machine control using nine-switch inverter for multi-drive systems,” in *Proc. IEEE 12th Int. Conf. Comput., Power Electron. Power Eng.*, Apr. 2018, pp. 1–6.

[13] S. Vazquez, J. Rodriguez, M. Rivera, L. G. Franquelo, and M. Norambuena, “Model predictive control for power converters and drives: Advances and trends,” *IEEE Trans. Ind. Electron.*, vol. 64, no. 2, pp. 935–947, Feb. 2017.

[14] S. Kouro, P. Cortes, R. Vargas, U. Ammann, and J. Rodriguez, “Model predictive control—A simple and powerful method to control power converters,” *IEEE Trans. Ind. Electron.*, vol. 56, no. 6, pp. 1826–1838, Jun. 2009.

[15] J. Rodriguez, R. M. Kennel, J. R. Espinoza, M. Trincado, C. A. Silva, and C. A. Rojas, “High-performance control strategies for electrical drives: An experimental assessment,” *IEEE Trans. Ind. Electron.*, vol. 59, no. 2, pp. 812–820, Feb. 2012.

[16] P. Acuna, L. Moran, M. Rivera, R. Aguilera, R. Burgos, and V. G. Agelidis, “A single-objective predictive control method for a multivariable single-phase three-level NPC converter-based active power filter,” *IEEE Trans. Ind. Electron.*, vol. 62, no. 7, pp. 4598–4607, Jul. 2015.

[17] J.-W. Moon, J.-S. Gwon, J.-W. Park, D.-W. Kang, and J.-M. Kim, “Model predictive control with a reduced number of considered states in a modular multilevel converter for HVDC system,” *IEEE Trans. Power Del.*, vol. 30, no. 2, pp. 608–617, Apr. 2015.

[18] A. S. Lunardi, J. S. S. Chaves, and A. J. S. Filho, “Predictive direct torque control for a squirrel cage induction generator grid connected for wind energy applications,” *IEEE Latin Amer. Trans.*, vol. 14, no. 11, pp. 4454–4461, Nov. 2016.

[19] F. Wang, S. Li, X. Mei, W. Xie, J. Rodriguez, and R. M. Kennel, “Model-based predictive direct control strategies for electrical drives: An experimental evaluation of PTC and PCC methods,” *IEEE Trans. Ind. Informat.*, vol. 11, no. 3, pp. 671–681, Jun. 2015.

[20] S. S. Lee, Y. E. Heng, and M. A. Roslan, “Finite control set model predictive control of nine-switch AC/DC/AC converter,” in *Proc. IEEE Int. Conf. Power Energy*, Nov. 2016, pp. 746–751.

[21] J. Rodriguez *et al.*, “State of the art of finite control set model predictive control in power electronics,” *IEEE Trans. Ind. Informat.*, vol. 9, no. 2, pp. 1003–1016, May 2013.

[22] F. Wang, X. Mei, J. Rodriguez, and R. Kennel, “Model predictive control for electrical drive systems—An overview,” *CES Trans. Elect. Mach. Syst.*, vol. 1, no. 3, pp. 219–230, 2017.

[23] Y. Zhang, W. Xie, Z. Li, and Y. Zhang, “Model predictive direct power control of a PWM rectifier with duty cycle optimization,” *IEEE Trans. Power Electron.*, vol. 28, no. 11, pp. 5343–5351, Nov. 2013.

[24] Y. Zhang and H. Yang, “Model predictive torque control of induction motor drives with optimal duty cycle control,” *IEEE Trans. Power. Electron.*, vol. 29, no. 12, pp. 6593–6603, Dec. 2014.

[25] Z. Song, Y. Tian, W. Chen, Z. Zou, and Z. Chen, “Predictive duty cycle control of three-phase active-front-end rectifiers,” *IEEE Trans. Power Electron.*, vol. 31, no. 1, pp. 698–710, Jan. 2016.

[26] X. Zhang, L. Tan, J. Xian, and H. Zhang, “Three vector complete model predictive control for three-phase grid-connected inverters with LCL filter,” in *Proc. 13th IEEE Conf. Ind. Electron. Appl.*, May 2018, pp. 1470–1475.

[27] H. Gao, B. Wu, and D. Xu, “Nine-switch AC/AC current source converter for microgrid application with model predictive control,” *IET Power Electron.*, vol. 10, no. 13, pp. 1759–1766, Oct. 2017.

[28] S. S. Lee and Y. E. Heng, “Predictive control of power flow between two islanded microgrids using nine-switch converter,” *J. Renewable Sustain. Energy*, vol. 8, no. 5, 2016, Art. no. 055502.

[29] O. Gulbudak and E. Santi, “Model predictive control of dual-output nine-switch inverter with output filter,” in *Proc. IEEE Energy Convers. Congr. Expo.*, Sep. 2015, pp. 1582–1589.

[30] V. Jayan and A. Ghias, “Finite control set model predictive control of a nine switch dual output converter as a power quality conditioner,” in *Proc. IEEE Int. Conf. Ind. Technol.*, Feb. 2019, pp. 1241–1246.

[31] P. R. U. Guazzelli *et al.*, “Dual predictive current control of grid connected nine-switch converter applied to induction generator,” in *Proc. 13th IEEE Int. Conf. Ind. Appl.*, 2018, pp. 1038–1044.

[32] O. Gulbudak and M. Gokdag, “Asymmetrical multi-step direct model predictive control of nine-switch inverter for dual-output mode operation,” *IEEE Access*, vol. 7, pp. 164720–164733, 2019.

[33] P. Vas, *Vector Control of AC Machines* (Monographs in Electrical and Electronic Engineering). Oxford, U.K.: Clarendon, 1990.

[34] S. Golestan, J. M. Guerrero, and J. C. Vasquez, “Three-phase PLLs: A review of recent advances,” *IEEE Trans. Power. Electron.*, vol. 32, no. 3, pp. 1894–1907, Mar. 2017.

[35] S. Golestan, M. Ramezani, J. M. Guerrero, F. D. Freijedo, and M. Monfared, “Moving average filter based phase-locked loops: Performance analysis and design guidelines,” *IEEE Trans. Power Electron.*, vol. 29, no. 6, pp. 2750–2763, Jun. 2014.

[36] P. Karamanakos, T. Geyer, and R. Kennel, "On the choice of norm in finite control set model predictive control," *IEEE Trans. Power Electron.*, vol. 33, no. 8, pp. 7105–7117, Aug. 2018.

[37] P. Cortes, J. Rodriguez, C. Silva, and A. Flores, "Delay compensation in model predictive current control of a three-phase inverter," *IEEE Trans. Ind. Electron.*, vol. 59, no. 2, pp. 1323–1325, Feb. 2012.

[38] F. Wang, Z. Chen, P. Stolze, J.-F. Stumper, J. Rodriguez, and R. Kennel, "Encoderless finite-state predictive torque control for induction machine with a compensated MRAS," *IEEE Trans. Ind. Informat.*, vol. 10, no. 2, pp. 1097–1106, May 2014.

[39] X. Li, L. Qu, B. Zhang, G. Zhang, and H. Liao, "A simplified modulation strategy of nine-switch inverter to cut off half of switching modes," *IEEE Access*, vol. 6, pp. 7254–7261, 2018.

Paulo Roberto Ubaldo Guazzelli received the B.E. (Hons.) degree in electrical engineering from the Federal University of São Carlos, São Carlos, Brazil, in 2014, and the M.Sc. and Ph.D. degrees from the University of São Paulo, São Carlos, Brazil, in 2017 and 2021, respectively.

He is currently a Postdoctoral Researcher with the University of São Paulo. His research interests include power electronics, electric machine drives, and model-predictive control.

Stefan Thiago Cury Alves dos Santos received the B.Eng. and M.Eng. degrees in 2017 and 2021, respectively, from the University of São Paulo, São Carlos, Brazil, where he is currently working toward the Ph.D. degree.

His research interests include control of electric machine drives, control systems, and power electronics.

Allan Gregori de Castro received the B.E. degree in electrical engineering from the Federal University of Technology—Paraná, Curitiba, Brazil, in 2014, and the M.Sc. degree in electrical engineering in 2017 from the University of São Paulo, São Carlos, Brazil, where he is currently working toward the Ph.D. degree in electrical engineering with the São Carlos School of Engineering.

He is currently a Researcher with Tecumseh Products Company, São Carlos. His research interests include power electronics and electric machine drives.

William César de Andrade Pereira received the M.Sc. and D.Sc. degrees in electrical engineering from the School of Engineering of São Carlos, University of São Paulo, São Carlos, Brazil, in 2014 and 2019, respectively.

He is currently a Design Engineer with WEG Drives and Controls, Jaraguá do Sul, Brazil. His current research interests include control of electric drives for electric vehicles.

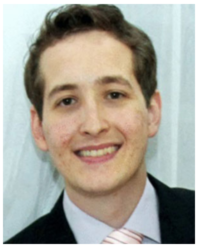

Carlos Matheus Rodrigues de Oliveira received the B.Eng. degree from the Federal University of Technology—Paraná, Apucarana, Brazil, in 2013, and the M.Eng. and Ph.D. degrees from the University of São Paulo, São Carlos, Brazil, in 2015 and 2019, respectively.

Since 2020, he has been a Professor with the Department of Electrical Engineering, Federal University of Technology—Paraná, in the areas of control, drives, and electrical machines. His research interests include control of electrical drive machines, dynamic load emulations, and power electronics.

José Roberto Boffino de Almeida Monteiro (Member, IEEE) received the bachelor's, master's, and Doctoral degrees in electrical engineering from the School of Engineering of São Carlos, University of São Paulo (USP), São Carlos, Brazil, in 1994, 1997, and 2002, respectively.

He is currently a Professor with the Department of Electrical Engineering, School of Engineering of São Carlos, USP, where he teaches power electronics and electric machines. His main research interests include electric machines, permanent magnet machines, power electronics, and control.

Manoel Luís de Aguiar received the B.Eng. degree from the Federal University of Uberlândia, Uberlândia, Brazil, in 1983, the master's degree from the Department of Electrical Engineering, School of Engineering of São Carlos, University of São Paulo (USP), São Carlos, Brazil, in 1987, and the Doctoral degree from the Institute of Electronics, Technical University of Berlin, Berlin, Germany, in 1994, all in electrical engineering.

Since 1986, he has been teaching with the Department of Electrical Engineering, School of Engineering of São Carlos, USP, in the areas of power electronics, machines and drivers, and control systems.